Comparative study of methods for counting of dislocations in 4H-SiC

Christian Kranert [a,*], Paul Wimmer [a], Alexis Drouin [b], Christian Reimann [a], Jochen Friedrich [a]

[a] *Fraunhofer IISB, Schottkystr. 10, 91058 Erlangen, Germany*
[b] *Soitec, Parc Technologique des Fontaines, Chemin des Franques, 38190 Bernin, France*

ARTICLE INFO

ABSTRACT

Three experimental techniques to determine the density of the three relevant dislocation types (basal plane, threading edge and threading screw) in SiC were investigated: etching by molten KOH with and without the addition of Na_2O_2 and X-ray topography. The applicability to implement these techniques for a reliable full-wafer scale analysis is tested experimentally. The limitations are found to be mainly determined by the feature sizes. Based on simple considerations, the range of acceptable sizes of the dislocation-related features is estimated. Etching with Na_2O_2 allows to distinguish between all three types of dislocations, but a reliable detection is difficult to set up due to a too large spread of etch pit size. Without the addition of Na_2O_2, TSD and TED cannot be distinguished, but etch pit sizes become more homogeneous, enabling robust etch pit detection over a wider range of dislocation densities. X-ray topography gives reliable results for TSDs and BPDs whereas the measurement of TEDs is limited.

1. Introduction

Silicon carbide (SiC) is becoming an increasingly important semiconductor material due to its striking benefits for application in power electronics [1,2] and the availability of native substrates with diameters of 150 mm and recently also 200 mm. Particularly in the booming sector of electric mobility, which requires devices with a breakdown voltage of typically 1.2 kV, SiC outperforms particularly silicon and therefore became a prime example of post-silicon technology.

However, whereas silicon can be produced so that it does not contain a single dislocation, SiC is far from being dislocation-free with typical dislocation densities in the order of 1×10^3 cm^{-2} to 1×10^4 cm^{-2}. Since these dislocations can affect the further processing as well as the performance and yield of the final devices [3–7], a characterization of the dislocation density and distribution is required in order to monitor the crystal growth process and to specify material quality for certain applications.

Historically, etching on the Si-face in alkaline melts, preferably KOH, has become the industry standard for quantifying dislocation densities of 4H-SiC wafers [8]. Unfortunately, for highly conductive n-doped SiC wafers, which cover almost the complete market for SiC wafers, it becomes impossible to distinguish between threading screw (TSD) and threading edge (TED) dislocations [9,10]. Since TSDs are considered to have a stronger impact on device performance, this distinction is highly desirable. This led to the development of different approaches like etching using a mixture of KOH and Na_2O_2 (KN)

[11,12], KOH and KO_2 [13], and analyzing the C-face of the SiC wafer after etching with KOH [14].

Regardless of which etching approach is applied, they all share common handicaps: Most obviously, etching is destructive, causing the loss of a highly valuable wafer after characterization, which also inhibits the further processing of the measured specimen. Further, keeping the results stable over time is a major challenge: The etchant may decay, small variations in melt temperature and etching time can cause critical variations in the etch pit sizes, potentially confusing the classification algorithm, and also the cleaning process after etching is a critical step as residuals may either cover etch pits or be mistakenly recognized as such.

X-ray (diffraction) topography (XRT, sometimes also referred to as X-ray diffraction imaging XRDI) [15–17] in general can prevent the problems of etching as it is non-destructive and directly images the strain field caused by the dislocations such that the measurement is independent of sample preparation and can be repeated many times, also to verify reproducibility and repeatability. Additionally, as opposed to etching methods, XRT gives direct information on the type of dislocation, since the Burgers vector can be accessed by applying the $\vec{g} \cdot \vec{b}$ and $\vec{g} \cdot \vec{b} \times \vec{L}$ criteria. In the past, these measurements required beam time at synchrotron facilities and often only small regions of the wafer could be analyzed. Using a special setup, the measurement of full SiC wafers at a synchrotron has been demonstrated [18]. With the availability of high-resolution lab-scale tools, similar measurement
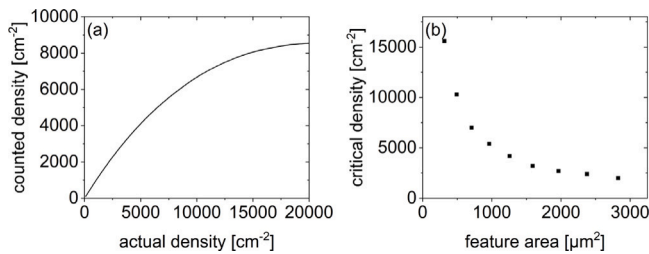

Fig. 1. (a) Simulated number of detected areas over the actual number of features for a feature diameter of $50\,\mu m$. (b) Critical density above which less than 90% of the actually placed features are found as separate areas in dependence on the feature area.

capabilities can now be introduced into laboratories and factories for routine full-wafer scale measurements [19,20].

Since all the above-mentioned options are available to fulfill the task of dislocation quantification, it is of great interest how these methods perform compared to each other. Even though publications exist that show the general feasibility of each method, a comparison for full wafer analysis is missing. The purpose of the present work is to fill this gap and compare the established approaches for dislocation quantification in SiC on full wafer scale: etching in KOH, etching in KN, and analysis using XRT. This comparison focuses only on the potential accuracy of defect detection, technical challenges as discussed above regarding stabilizing melt or how to cope with the surface of the wafer being destroyed by etching are tasks of optimization and implementation and might be more or less critical, depending on how things are realized in the industrial environment.

2. Theoretical considerations

For the methods discussed here, except for the BPD quantification by XRT, dislocation quantification is based on the counting of contrasts in an image. This is usually done in two process steps: segmentation and classification. Obviously, segmentation works best if the features to be quantified are well separated. Overlapping can be handled to a certain degree, but the more complex overlapping structures become, the less accurate any algorithm will become. Therefore, to obtain the best possible quantification, ideally clearly separated features are desired. Classification of the features is then limited by the number of classes, how well their appearance is separated and the amount of information that can be used for the classification. The better these requirements for segmentation and classification are fulfilled, the easier it is to develop a well-performing quantification algorithm. Whereas classification requires sufficiently large features that contain as much information as possible, too large features will cause overlapping and thus limit the quality of segmentation.

In order to assess an upper threshold for the feature size, we carried out Monte Carlo simulations of idealized cases. Round features with given diameter were placed randomly on a $1\,mm \times 1\,mm$ area. After the addition of each feature, the number of separate areas was counted similar to the approach setting a gray level threshold. For each feature size, 500 trials were run. We then arbitrarily define a limit for a decent segmentation: When the number of detected connected areas is less than 90% of the original round features, the overlapping is assumed to significantly impact the quality of segmentation. Of course, the actual impact will depend on the applied algorithm, but for our purposes the thereby obtained value only needs to serve as a measure of the "segmentability" of the resulting image.

The results of this simulation are shown in Fig. 1. As an example, Fig. 1(a) shows the simulated density of detected connected regions as compared to the actual feature density for a feature diameter of $50\,\mu m$ corresponding to a feature area of $1963\,\mu m^2$. Even at an actual density of $20\,000\,cm^{-2}$, only around $8500\,cm^{-2}$ connected areas are found.

The plot in Fig. 1(b) shows that the critical defect density drops strongly with increasing feature size. For a feature area of approx. $500\,\mu m^2$, the critical density is at approx. $10\,000\,cm^{-2}$, which is reduced to $2500\,cm^{-2}$ for features with an area of $2000\,\mu m^2$.

When moving towards a very small feature size, classification becomes more critical as the usable information decreases. Increasing the optical resolution is often not a feasible solution because measurement time and the amount of data to be analyzed will increase. If aiming for a full wafer analysis, a mapping of a full $150\,mm$ wafer with a pixel size of $1\,\mu m$ will result in 22.5×10^9 pixels. Therefore, this resolution can be assumed to be an upper limit. If one then, for example, requires 5×5 pixels for a sufficient classification quality, the minimum feature size should not be below $25\,\mu m$.

Summing up both requirements, one finds that the span of acceptable feature size depends on the expected dislocation density. Recent production-grade SiC wafers still reach local dislocation densities (dominantly TEDs) of around $10\,000\,cm^{-2}$, which would require the TED etch pit size (assuming no other defects to be present) to be not larger than $500\,\mu m^2$. The spread between etch pit sizes then should not be less than a factor of 20 so that also the smallest features can safely be classified.

3. Samples and methods

A total of eight wafers were analyzed from five leading SiC wafer manufacturers in order to rule out any specifics of a certain material and to cover a huge share of the market. All wafers were standard production grade $150\,mm$ wafers in compliance with SEMI M55 with nitrogen doping to achieve an n-type conductivity and a resistivity of approx. $20\,m\Omega\,cm$. The nominal offcut is $4°$. Four of the wafers (KN1 to KN4) were first etched externally in molten $KOH+Na_2O_2$ by Japan Fine Ceramics Center based on the original literature on this approach [11,12] and with the etching time adapted to the individual wafer based on a similar dummy wafer. The etching temperature was identical for all wafers. These wafers were subsequently measured by XRT where the TSD measurement was carried out on the C-face to avoid etch pits to affect the topograph quality.

The other four wafers (KOH1 to KOH4) were first measured by XRT and then etched using a standard KOH melt without Na_2O_2. Etching in KOH was carried out at $520\,°C$ for $12\,min$ to obtain a good compromise between overlapping and resolution of the etch pit size. The wafers were then analyzed using an Olympus MX-61 reflected light microscope equipped with an automated motorized stage using a $20\times$ objective. Measurements were carried out in bright field configuration without a DIC filter applied. Wafers etched by KN were analyzed the same way, but partially with lower magnification, depending on the actual etch pit size. The analysis was done using a classification algorithm based on gray level thresholding and feature analysis based on size and shape. The classification parameters (e.g. area, circularity, solidity, aspect ratio) were optimized individually for each sample to obtain the best possible selectivity.

X-ray topography measurements were carried out using a Rigaku XRTmicron system equipped with a 1.2 kW rotating anode (Cu/Mo) and a high resolution CCD detector (XTOP, pixel size $5.4\,\mu m$) operating in time-delay integration (TDI) mode for topographic scans. The setup implements the Lang method with a slightly divergent beam, both for Bragg ("reflection") and Laue case ("transmission"). For TSD detection, diffraction from the (0008) lattice planes was mapped with a scan speed of $30\,mm\,min^{-1}$. The TSDs were then counted using a fixed in-house algorithm. Quantification of BPDs was done based on topographs of the diffraction from the $(11\bar{2}0)$ lattice planes (with $\vec{g}$ parallel to the flat) mapped with a scan speed of $80\,mm\,min^{-1}$. The analysis of the BPD density uses the effect that each BPD contributes to the total diffraction intensity. Thus, the cumulative diffraction intensity of the BPDs was used as a measure for the BPD density. This value of arbitrary units was then calibrated against the BPD density distribution obtained from KOH etching of reference wafers. For TED analysis, the topographic scan of the diffraction from the $(22\bar{4}0)$ lattice plane was recorded with a measurement speed of $2.5\,mm\,min^{-1}$.
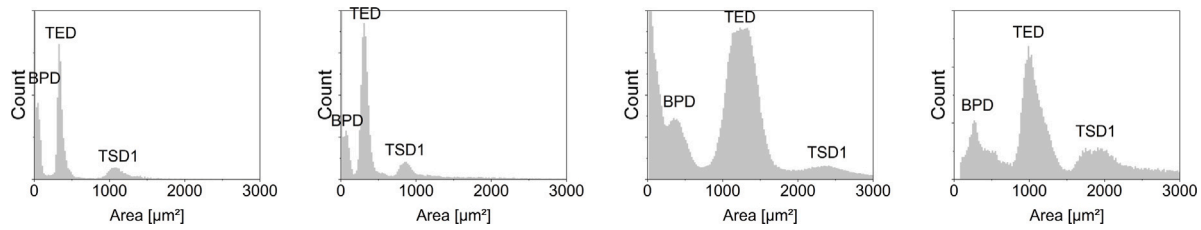
Fig. 2. Size distribution of the etch pits after KN etching for wafers KN1 to KN4 from left to right.

4. Results

4.1. KN vs. XRT

Generally, etch pits in SiC with the standard 4° offcut can be divided into two types: Oval and round etch pits. The former ones originate from dislocations running in the basal plane, i.e., BPDs, while the latter ones may originate from any form of threading dislocation (TD). When using the KN mixture as etchant, the round dislocations further split up by size: The etch pits of TEDs are the smallest etch pits, whereas TDs with c-component of their Burgers vector (mixed and screw) form larger etch pits which can be further divided into TSD1 and TSD2. To the knowledge of the authors, the origin for the different etch pit sizes has not yet been clarified and is not scope of the present work. For our purpose, the essential requirement is to distinguish between TSDs (which we here use synonymically to the sum of all threading screw and mixed dislocations) and TEDs. We therefore do not distinguish between TSD1 and TSD2 and just count the sum of both.

As an overview over the results of etching, the size distributions are shown in Fig. 2 for the four wafers etched using KN. The size distribution results from setting a gray scale threshold and counting all objects without any additional shape discrimination. Therefore, the plots also include misdetections of residuals, particles and so on.

Obviously, there are two classes of etch pit sizes: The wafers KN3 and KN4 have larger etch pits (TED: approx. $1200\,\mu m^2$, TSD: $2000\,\mu m^2$ ...$2500\,\mu m^2$) than the other ones (TED: approx. $400\,\mu m^2$, TSD: approx $1000\,\mu m^2$). These differences nicely allow to investigate the impact of the etch pit size on the overlapping for the here applied defect analysis. From the deliberations in Section 2, the critical defect densities for the first group are $4400\,cm^{-2}$ TEDs and $2500\,cm^{-2}$ for TSDs, and for the second group $12\,000\,cm^{-2}$ and $5200\,cm^{-2}$, respectively. Of course, if both types of dislocations occur at the same region, the actual limit will be lower.

Based on the clear separation of etch pits from TEDs and TSDs, the classification algorithm was set up to obtain a full-wafer scale analysis of the wafers. Additional shape descriptors were added mainly to distinguish etch pits from any other object that might be visible after thresholding. These dislocation distributions were then compared to the results from XRT acquired from the same wafers.

The TSD features in the XRT measurements have a size of approx. $2000\,\mu m^2$, which yields a critical dislocation density of approx. $2500\,cm^{-2}$. Since in production-grade material as in the wafers investigated here, typically no other defects are visible in high quantities, this value is not reduced by the occurrence of these other defects.

The results of the comparison between KN etching and XRT can be put in the same two groups as the etch pit size distributions. For the wafers KN1 and KN2 with the smaller etch pits, there was a very good agreement of the TSD distribution between KN etching and XRT measurements, both qualitatively and quantitatively (see exemplarily for KN1 in Fig. 3(a) and (b)). Local deviations were especially observed in regions with high BPD and/or TED density where the TSD density detected from the KN analysis was lower than for the XRT results. The BPD density showed a good agreement as well with slightly lower BPD density reported for KN etching, which is at least partly expected due
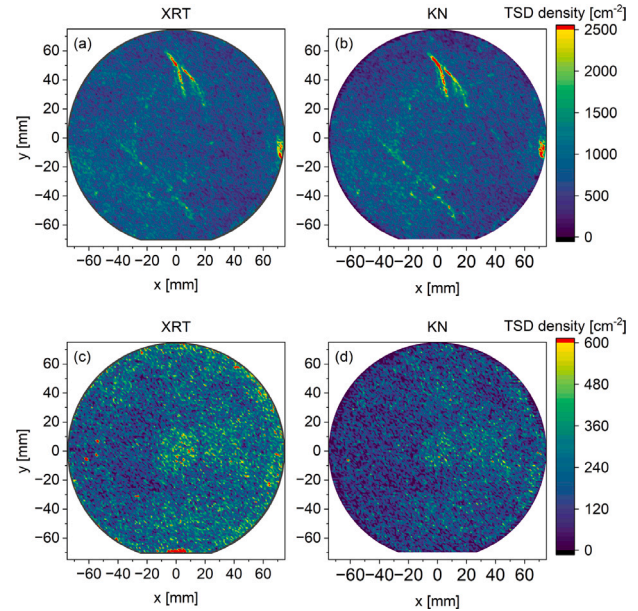

Fig. 3. TSD density maps for wafers KN1 ((a) and b) and KN3((c) and (d)). The TSD density determined by XRT and KN etching is shown on the left ((a) and (c)) and right ((b) and (d)), respectively.

to etch pit overlapping in regions of high defect density (see Fig. 4(a) and (b)). The results are very similar for the wafer KN2 (not shown).

The results are significantly different for the wafers KN3 and KN4 which had larger etch pits. Qualitatively, the TSD density distribution shows a very good agreement between KN and XRT measurements (see Fig. 3(c) and (d) for wafer KN3). However, the measured absolute densities are significantly lower for the KN measurement, which is attributed again to etch pit overlapping. The differences are even more significant for the BPD measurements shown exemplarily for the wafer KN4. Since this wafer exhibits very high BPD densities above $1 \times 10^4\,cm^{-2}$ in some regions around the edge, etch pit counting struggles with the strong overlap of etch pits, resulting in a severe underreporting of BPD density. Also XRT shows problems for this particular wafer, which originate from a very strong lattice curvature in the regions of high BPD density. This is a result of the requirement to meet the Bragg condition for the full X-ray beam during the measurement and results in an underreporting of BPD density for the XRT measurement in regions with a lattice curvature larger than about $10\,km^{-1}$. This issue is not present for the wafer KN3 (not shown): Here, the BPD distribution shows a again a good qualitative agreement between XRT and KN with lower absolute values for KN etching, particularly in regions of high overall dislocation density where an overlap is most likely.

Mean values for the dislocation densities are summarized in Table 1. TSD densities are in good agreement for the wafer KN1 due to the small etch pit sizes and moderate dislocation densities. The differences are larger for wafers KN3 and KN4 due to the large etch pits and for KN2 due to the higher dislocation density. In all cases, XRT reported higher
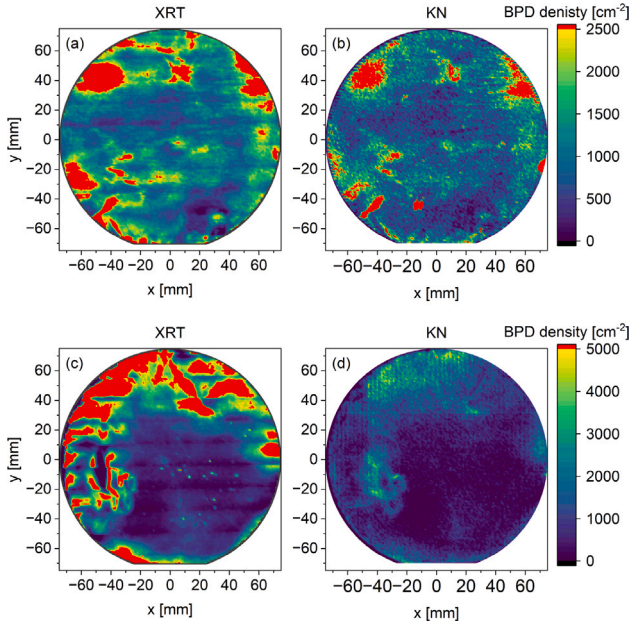
Fig. 4. BPD density maps for wafers KN1 ((a) and (b)) and KN4 ((c) and (d)). The BPD density determined by XRT and KN etching is shown on the left ((a) and (c)) and right ((b) and (d)), respectively.

TSD densities, in agreement to the assumption that the deviations result from undercounting of etch pits due to overlapping. For the BPD density, again an acceptable agreement between both methods is observed for wafers KN1 and KN2, whereas there is a dramatic undercounting of BPDs for wafer KN4 due to the combination of high BPD density and large etch pits. This undercounting is even more severe than the underestimation from the XRT measurements caused by the strong lattice curvature. For wafer KN3, the difference is moderate despite the large etch pits, due to the low overall etch pit density which limits overlapping. The slightly larger values observed in the XRT measurement can also, at least partially, be attributed to the etched surface and thinned wafer.

4.2. KOH vs. XRT

Since TSDs and TEDs cannot be distinguished from their etch pit sizes when applying pure KOH melt to highly doped substrates, the focus of the comparison between KOH and XRT was mainly on BPDs. Additionally, we tested the possibility to also detect TED by XRT based on a low-BPD sample.

The etching conditions were chosen to obtain the smallest etch pits which were still large enough to distinguish round etch pits from TSDs/TEDs, oval etch pits from BPDs and stains on the sample. This led to a typical etch pit size for TEDs of around $200\,\mu m^2$. The etch pits for BPD were only slightly smaller and only a fraction of the TSDs led to etch pits larger than $500\,\mu m^2$. Thereby, etch pit overlapping was only an issue in regions of very high etch pit density or clustering, in agreement to the estimations in Section 2.

The BPD density distribution obtained by KOH etching and the XRT measurements are shown in Fig. 5. This time, a good overall agreement can be observed for all three wafers. Problems with the wafer curvature affecting the XRT measurements were not observed. For KOH etching, etch pit overlap was marginal so that these two error sources observed for the comparison between XRT and KN etching were ruled out.

Other problems were mainly observed for the KOH-etched samples: The reported BPD density in the upper right quarter of the wafer is slightly lower than for the XRT measurements, particularly for wafers
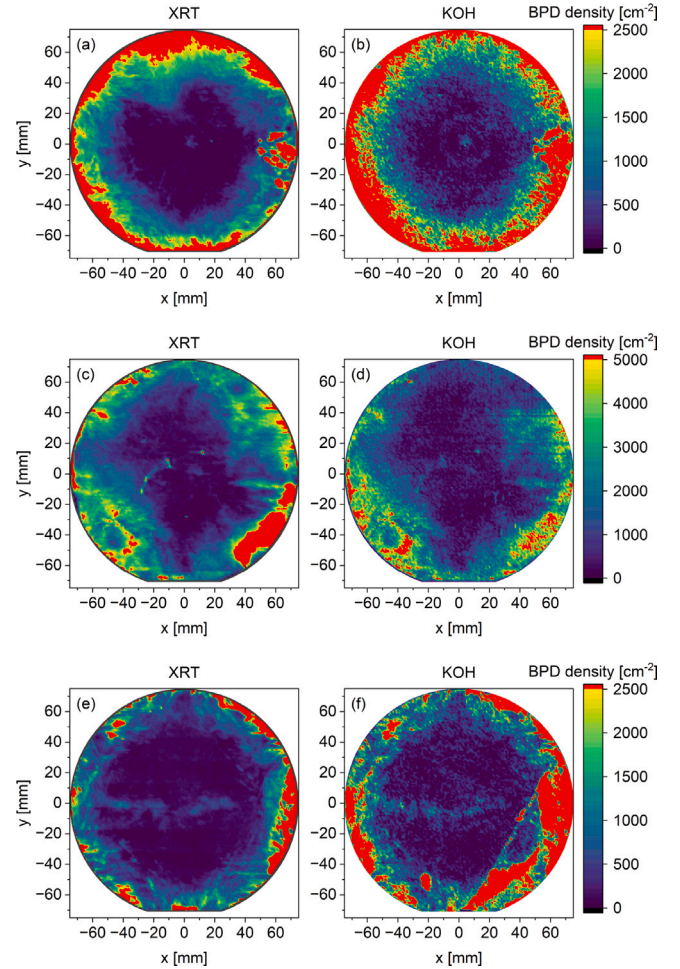

Fig. 5. BPD density maps for wafers KOH1 ((a) and (b)), KOH2 ((c) and (d)) and KOH3 ((e) and (f)). The BPD density determined by XRT and KOH etching is shown on the left ((a), (c), and (e)) and right ((b), (d), and (f)), respectively.

Table 1
Mean dislocation densities in cm^{-2} as measured by KN etching and XRT, respectively.

Wafer	TSD		BPD		TED
	KN	XRT	KN	XRT	KN
KN1	753	768	1098	1420	1345
KN2	1099	1349	2791	2693	3190
KN3	158	223	314	420	1048
KN4	589	823	850	2455	2642

KOH1 and KOH2. In this region, we observe a blurring of the microscope image, probably caused by a slight vibration of the motorized stage. Due to the blurring, many etch pits were not counted as verified by a visual inspection. Taking into account these systematic deviations, the agreement of the mean dislocation densities over the wafer area as given in Table 2 is very good. For wafer KOH3, the lower right part was broken off and could not undergo the same cleaning procedure as the remaining part of the wafer, causing a high number of misdetections in this region. To avoid this region from affecting the quantitative comparison, it was excluded from the mean values given in Table 2. However, also in the remaining part of the wafer, there are a few regions which were influenced by stains, particularly at $(-20\,mm, -50\,mm)$ and at the left edge. Due to the generally very low BPD density, these regions cause a rather strong deviation between both methods.

The possibilities of TED measurement by XRT are strongly limited because TED and BPD share the Burgers vectors in the *c*-plane. Since BPDs extend over a large area, already a BPD density corresponding

Table 2
Mean BPD densities in cm^{-2} as measured by KOH etching and XRT, respectively.

	KOH	XRT
A2	1263	1389
B2	1513	1833
F2	702	443
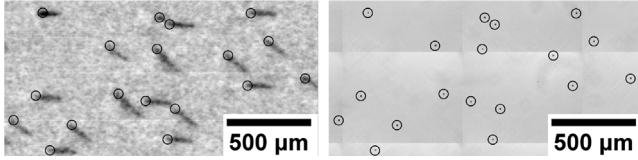
Fig. 6. Local sample showing TEDs in the XRT scan of the $(22\bar{4}0)$ reflection and after KOH etching. The circles indicate the automatically detected positions of TD-related etch pits projected onto the topograph and the microscope image, respectively.

Fig. 7. TD densities obtained from feature counting based on an XRT scan (sum of TEDs and TSDs from two different scans) and a microscope scan after KOH etching, respectively.

Fig. 8. Etch pits formed by KN etching in a region of increased dislocation density of wafer KN1 (left) and a region of similar etch pit density after KOH etching for wafer KOH2 (right).

to a small etch pit density will cause segmentation problems for TED analysis. Further, TEDs will not be visible for XRT measurements in Bragg configuration because of the small in-plane component of the $\vec{g}$-vector in this geometry and the low general contrast produced by TEDs. Therefore, another SiC wafer KOH4 with a very low mean BPD density below $200\,cm^{-2}$ and a large, nearly BPD-free area in the wafer center was analyzed and measured by XRT using diffraction from the $(22\bar{4}0)$ lattice plane in Laue configuration.

A local example of the agreement between etching result and XRT measurement is shown in Fig. 6. Obviously, the TEDs do not appear as spots in the X-ray topograph, but as short lines. There are two reasons for that: In order to match the Bragg conditions, the detector angle is not normal to the sample surface causing diffracted X-rays from the bottom of the sample to be projected more to the right side of the detector than the those from top. Second, TEDs are also not always perfectly propagating in the [0001]-direction, resulting in different orientations of the observed lines [21]. The comparison to the etch pit distribution shows that the intersection points with the surface correlate well with the left end of the lines visible in the topograph.
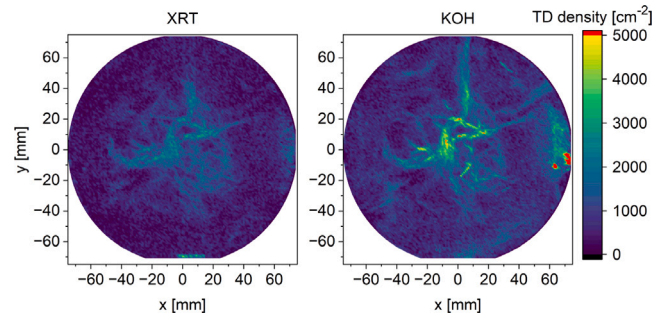
Due to the elongation of the contrast, the TEDs cover an area of typically around $3000\,\mu m^2$ in the topograph. From the considerations in Section 2, the critical defect density is then already reached at $2000\,cm^{-2}$, given that no BPDs are present. This agrees well with the results we obtain when applying a defect detection algorithm to the X-ray topograph, which are shown in Fig. 7: The distribution of TDs is in good agreement between the two techniques, with the absolute densities measured by XRT being significantly lower. These discrepancies are most pronounced in regions with high TED densities and near the wafer edge. In regions with high TED densities, overlapping of different TEDs causes an undercounting using the XRT technique, whereas near the edge the presence of BPDs causes TEDs being covered by BPDs. In regions with TED densities below $2000\,cm^{-2}$ and BPD densities below $10\,cm^{-2}$ a very good agreement has been observed, in accordance to the predictions of Section 2.

5. Discussion

The deviations between the different measurement techniques that we observe in this study clearly show the challenge of dislocation quantification in SiC substrates: While all of the tested techniques perform well within their limitations, setting up a defect quantification that is working reliably on the full wafer scale can be a different story.

5.1. KN etching

Etching using KOH + Na_2O_2 reliably gives etch pits with distinct properties for BPD, TED and TSD and further allows a distinction of
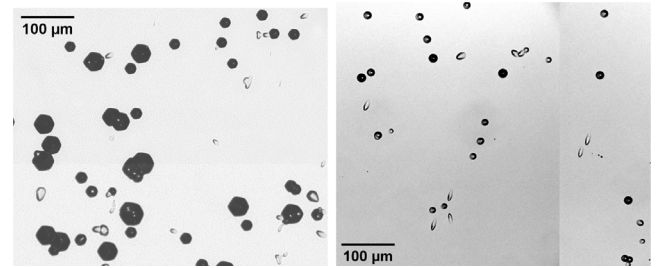
two types of TSDs. From a comparison to XRT we confirmed that the distinction between TSD and TED works well. However, the practical implementation suffered from the large variability of the etch pit sizes as discussed in Section 2. The optimum between etch pits becoming too large and overlap and etch pits becoming too small to be detected reliably becomes thinner. Therefore, the wafers with the larger etch pits clearly suffer from etch pit overlapping. This problem was also observed for wafers with the smaller etch pit sizes, but then only in regions of locally high etch pit density. This problem is illustrated in Fig. 8 showing a local image of wafer KN1. Here, one can see on the one hand etch pits that are extremely small, particularly of BPDs, and thus pose high requirements to the dislocation detection algorithm. Also, the etch pits of BPDs cover a wide range of possible appearance. Independent of the nature of dislocation detection algorithm, the reliability of the detection is always better the more homogeneous the features are. On the other hand, Fig. 8 also shows etch pits which are strongly overlapping, again posing additional challenges to the defect counting algorithm. Changing the etch pit size in either direction will always trade benefits at the one end for drawbacks at the other one. Therefore, even though KN in general enables a very accurate classification of the etch pits, a reliable implementation of this is a huge challenge and must be a compromise between detection of the smaller BPDs and separation between nearby etch pits. A good detection of etch pits as indicated in Table 3 is only achieved for typical defect densities in SiC if the etch pit size is similar to what we observed for samples KN1 and KN2 and at the same time if the image resolution is high enough to resolve also the smallest BPDs. Note that we generated about 100 GB of microscope data per wafer and were just able to resolve the also the small BPDs.

5.2. KOH etching

Etching in pure KOH melt has the fundamental limitation that TSD and TED cannot be distinguished due to the homogeneous etch pit sizes. However, as compared to KN etching, this has the benefit that it is easier to adjust the etching parameters to obtain both sufficiently large

Table 3
General assessment of detectability of the defect types by the three methods under investigation.

	KN	KOH	XRT
TSD	Good[a]	No	Good (<2500 cm^{-2})
TED	Good[a]	Good	Partially (near 0 BPDs)
BPD	Good[a]	Good	Good

[a] The assessment for KN etching is only valid for etch pit sizes as for wafers KN1 and KN2 and sufficiently high resolution microscope imaging.

etch pits and avoid etch pit overlapping. This difference is clearly seen by comparing the two examples in 8, where BPDs are larger and at the same time TDs are smaller than for KN etching. Thereby, this method appears to be beneficial particularly for BPD counting. In the typical case that the TSD density is much lower than the TED density, or if subtracting the TSD density measured by XRT, the TED density can be evaluated similarly well as with KN etching. For higher TSD densities, subtracting these values obviously becomes mandatory, canceling out the benefit of KOH etching being less prone to etch pit overlap in this case than KN etching with its larger TSD etch pits.

5.3. XRT

The application of XRT benefits from its non-destructive method already in that sense that one can use different measurement modes for different defects. There were approaches claiming to determine TSD, BPD and TED density from a single topographic scan using either (11$\bar{2}$0) or (11$\bar{2}$8) reflections, but the agreement of these approaches to other techniques was poor, which can be easily understood based on the expected heavy overlapping of defects at typical defect densities in SiC. When using the (0008) reflection, TSDs can be counted as easily and reliably as etch pits, resulting in a very good agreement to what is also obtained by KN etching with reasonable etch pit size. Overlapping obviously can also be an issue for the TSD density measurement by XRT due to its much lower resolution as for optical microscopes. This overlapping then again limits the linearity of the TSD density detection for densities above approx. 2500 cm^{-2}. At higher values, undercounting will also play a role for this technique.

The measurements of BPD densities underly the premise that the results need to be compatible to etch pit densities, leaving only a calibrated approach which has some inherent shortcomings: Besides being an indirect method, the absolute values cannot be better than those obtained from the etching method. As discussed above, KOH etching has benefits over KN etching for the purpose as being used as a reference method, but still is not perfect. Nevertheless, this does not affect relative values between wafers and thus XRT's applicability for wafer testing. When taking into account the uncertainties introduced by the reference method, the agreement between the BPD density measured by XRT and the etching techniques observed in this study can be assessed as very good.

The detection of TEDs is still a major challenge. For high BPD densities, the overlap with BPDs covers them completely. For wafers or regions with vanishing BPD density, which will become more important with improving crystal quality, the TEDs can be made visible and then agree well with what is found by KOH etching. However, for high TED densities, quantification will remain difficult due to overlapping of the TEDs with each other.

A potential source of error for XRT measurements is the lattice curvature. The TSD measurements are more tolerant because intensity variations can be leveled out much easier by a background correction, but BPD measurements are very sensitive to this issue. Most of the recent production-grade wafers exhibit a much lower wafer curvature, but still some examples exist like shown here were this can become a problem. However, particularly for BPD measurements, recently a modification of the XRT equipment using a wider beam divergence was proposed, which is supposed to solve this issue [20].

6. Conclusions

All three measurement techniques discussed here have their advantages and disadvantages: KN etching is the only method that allows to distinguish between all three defect types (TSD, TED and BPD), but actually implementing a routine capable of reproducibly doing so in an automated way is highly challenging due to the large spread in etch pit sizes on the same wafer, at least if wafers or regions with elevated dislocation density are to be analyzed. KOH etching trades in the distinction between TSD and TED for an easier to set up and more reliable dislocation detection. For the detection of TSDs, XRT appears to be the method of choice because of the possibility to blank out other defects. For BPD quantification, XRT seems to be on par with KOH etching and superior to KN etching, beyond its advantages of being non-destructive and preventing problems of melt stability. For TED measurements, KOH etching, potentially combined with the TSD measurement by XRT, shows the best performance with a slight advantage over KN etching. XRT can become more useful also for this question when the BPD density in production-grade wafers is further reduced.

CRediT authorship contribution statement

Christian Kranert: Conceptualization, Formal analysis, Investigation, Writing – original draft. **Paul Wimmer:** Formal analysis, Methodology, Writing – original draft. **Alexis Drouin:** Conceptualization, Resources. **Christian Reimann:** Conceptualization, Funding acquisition, Supervision, Writing – review & editing. **Jochen Friedrich:** Funding acquisition, Supervision.

Declaration of competing interest

The authors declare that they have no known competing financial interests or personal relationships that could have appeared to influence the work reported in this paper.

Data availability

The data that has been used is confidential.

References

[1] B. Jayant Baliga, Silicon carbide power devices, in: Springer Handbook of Semiconductor Devices, Springer, Cham, 2023, pp. 491–523.

[2] C.R. Eddy, D.K. Gaskill, Materials science. Silicon carbide as a platform for power electronics, Science (New York, N.Y.) 324 (5933) (2009) 1398–1400.

[3] R.A. Berechman, M. Skowronski, S. Soloviev, P. Sandvik, Electrical characterization of 4H–SiC avalanche photodiodes containing threading edge and screw dislocations, J. Appl. Phys. 107 (11) (2010).

[4] A.G. Chynoweth, G.L. Pearson, Effect of dislocations on breakdown in silicon p-n junctions, J. Appl. Phys. 29 (7) (1958) 1103–1110.

[5] Hirokazu Fujiwara, Hideki Naruoka, Masaki Konishi, Kimimori Hamada, Takashi Katsuno, Tsuyoshi Ishikawa, Yukihiko Watanabe, Takeshi Endo, Relationship between threading dislocation and leakage current in 4H-SiC diodes, Appl. Phys. Lett. 100 (24) (2012).

[6] P.G Neudeck, W. Huang, M. Dudley, Breakdown degradation associated with elementary screw dislocations in 4H-SiC p+n junction rectifiers, Solid-State Electron. 42 (12) (1998) 2157–2164.

[7] M. Skowronski, S. Ha, Degradation of hexagonal silicon-carbide-based bipolar devices, J. Appl. Phys. 99 (1) (2006).

[8] Masakazu Katsuno, Noboru Ohtani, Jun Takahashi, Hirokatsu Yashiro, Masatoshi Kanaya, Mechanism of molten KOH etching of SiC single crystals: Comparative study with thermal oxidation, Japan. J. Appl. Phys. 38 (8R) (1999) 4661.

[9] B. Kallinger, S. Polster, P. Berwian, J. Friedrich, G. Müller, A.N. Danilewsky, A. Wehrhahn, A.-D. Weber, Threading dislocations in n- and p-type 4H–SiC material analyzed by etching and synchrotron X-ray topography, J. Cryst. Growth 314 (1) (2011) 21–29.

[10] Ping Wu, Murugesu Yoganathan, Ilya Zwieback, Yi Chen, Michael Dudley, Characterization of dislocations and micropipes in 4h n⁺ SiC substrates, Mater. Sci. Forum 600–603 (2008) 333–336.

[11] Yongzhao Yao, Yukari Ishikawa, Yoshihiro Sugawara, Koji Sato, Katsunori Danno, Hiroshi Suzuki, Takeshi Bessho, Satoshi Yamaguchi, Koichi Nishikawa, Correlation between etch pits formed by molten koh+na2o2 etching and dislocation types in heavily doped n+-4H–SiC studied by X-ray topography, J. Cryst. Growth 364 (2013) 7–10.

[12] Yong-Zhao Yao, Yukari Ishikawa, Yoshihiro Sugawara, Hiroaki Saitoh, Katsunori Danno, Hiroshi Suzuki, Yoichiro Kawai, Noriyoshi Shibata, Molten KOH etching with na2o2 additive for dislocation revelation in 4H-SiC epilayers and substrates, Japan. J. Appl. Phys. 50 (7R) (2011) 075502.

[13] Moonkyong Na, In Ho Kang, Jeong Hyun Moon, Wook Bahng, Role of the oxidizing agent in the etching of 4H-SiC substrates with molten KOH, J. Korean Phys. Soc. 69 (11) (2016) 1677–1682.

[14] Joseph J. Sumakeris, R.T. Leonard, Eugene Deyneka, Yuri Khlebnikov, Adrian R. Powell, Jeff Seaman, Michael J. Paisley, V. Tsevtkov, Jian Qiu Guo, Yu Yang, Michael Dudley, Elif Balkas, Dislocation characterization in 4H-SiC crystals, Mater. Sci. Forum 858 (2016) 393–396.

[15] Brian Keith Tanner, X-Ray Diffraction Topography, First edition, in: Pergamon international library, vol. 10, Pergamon Press, Oxford, England, 1976.

[16] André Authier, X-Ray and Neutron Dynamical Diffraction: Theory and Applications, in: Nato Science Series B, vol. 357, Springer, New York, NY, 1996.

[17] Balaji Raghothamachar, Michael Dudley, X-Ray Topography, 2019.

[18] Stanislav Stoupin, Balaji Raghothamachar, Michael Dudley, Zunping Liu, Emil Trakhtenberg, Keenan Lang, Kurt Goetze, Joseph Sullivan, Albert Macrander, Projection x-ray topography system at 1-BM x-ray optics test beamline at the advanced photon source, AIP Conf. Proc. 1741 (1) (2016) 050018.

[19] K. Omote, Crystal defects in SiC wafers and a new X-ray topography system, Rigaku J. 29 (1) (2013) 1–8.

[20] C. Kranert, C. Reimann, Y. Ueji, K. Shimamoto, K. Omote, Scrutinising SiC with X-ray topography, Compound Semicond. 29 (2) (2023) 18–23.

[21] Ping Wu, Etching study of dislocations in heavily nitrogen doped SiC crystals, J. Cryst. Growth 312 (8) (2010) 1193–1198.